Analysis and Optimization of High-Frequency Switching Oscillation Conducted CM Current Considering Parasitic Parameters Based on a Half-Bridge Power Module

Qingshou Yang, *Student Member, IEEE*, Laili Wang, *Senior Member, IEEE*, Zhiyuan Qi, *Student Member, IEEE*, Xiaohui Lu, *Student Member, IEEE*, Zaojun Ma, *Student Member, IEEE*, Fengtao Yang, *Student Member, IEEE*, and Haihua Wang, *Student Member, IEEE*

***Abstract*—SiC MOSFETs with antiparallel SiC schottky barrier diodes (SBDs) without reverse recovery can significantly reduce turn-ON switching loss. However, this will exacerbate the oscillation during the switching process, making the electromagnetic interference problem more serious. This article analyzes the influence of the power module parasitic parameters on the propagation path and proposes the optimization principle for the first time. First, the high-frequency switching oscillation noise source (HO-S) and the propagation path considering power module parasitic parameters based on a double-pulse test circuit are analyzed. Second, a high-frequency switching oscillation conduction common-mode (HO-CM) current mathematical model is established during the switching oscillation process to clarify the relationship among noise source, propagation path, and HO-CM current. Then, in order to reduce HO-CM current, the optimization principle of HO-CM current excited by HO-S is proposed. The HO-CM current can be canceled by optimizing the power module layout or Busbar parasitic inductance. Finally, the effect of power module parasitic parameters on HO-CM current is verified, and the HO-CM currents of power modules with different packaging layouts are compared. This method can reduce the HO-CM current spectrum of the critical conduction mode or discontinuous conduction mode buck converter by more than 10 dB. The analysis of the effect of power module parasitic parameters on HO-CM current can guide power module layout design or power module selection based on different working conditions of half-bridge converters.**

***Index Terms*—Common-mode current, electromagnetic interference (EMI), optimization, oscillation, parasitic parameters.**

NOMENCLATURE

C_{D}	Output capacitance of the upper devices.
C_{oss}	Output capacitance of the lower devices.
C_1, C_2, C_3	Parasitic capacitances of power modules.
C_{dc}	Decoupling capacitance with low parasitic inductance.
C_{Y1}, C_{Y2}, C_{Y3}	C_1, C_2, C_3 by Y–△ transformation.
L_1, L_2, L_{s1}, L_{s2}	Parasitic inductances of power modules.
V_{D}	Drain–source voltage of the upper devices.
V_{ds}	Drain–source voltage of the lower devices.
i_{d}	Current of parasitic inductance L_1.
C_{12}	Sum of C_1 and C_2.
C_{23}	Sum of C_2 and C_3.
C_{13}	Sum of C_1 and C_3.
C_{123}	Sum of C_1, C_2, and C_3.
L_{12}	Sum of L_1 and L_2.
L_{s12}	Sum of L_{s1} and L_{s2}.
C_{Y13}	Sum of C_{Y1} and C_{Y3}.
C_{Y23}	Sum of C_{Y2} and C_{Y3}.
C_{DY1}	Sum of C_{D} and C_{Y1}.
C_{DY13}	Sum of C_{D}, C_{Y1}, and C_{Y3}.
C_{ossY3}	Sum of C_{oss} and C_{Y3}.
C_{ossY23}	Sum of C_{oss}, C_{Y2}, and C_{Y3}.
L_{sum}	Sum of L_1, L_2, L_{s1}, and L_{s2}.
p_1	L_1 divided by L_{s1}.
p_2	L_2 divided by L_{s1}.
p_3	L_{s2} divided by L_{s1}.
p	Sum of p_1 and p_2.
m	C_2 divided by C_1.
n	C_2 divided by C_3.
q	C_1 divided by C_3.

Manuscript received 15 March 2023; revised 16 May 2023; accepted 22 June 2023. Date of publication 5 July 2023; date of current version 1 September 2023. This work was supported in part by the fund of the National Natural Science Foundation of China under Grant U1966212. Recommended for publication by Associate Editor M. Hartmann. *(Corresponding author: Laili Wang.)*

The authors are with the State Key Laboratory of Electrical Insulation and Power Equipment, Xi'an Jiaotong University, Xi'an 710049, China (e-mail: qs_yang@stu.xjtu.edu.cn; llwang@mail.xjtu.edu.cn; mambaqizhy@stu.xjtu.edu.cn; lu2504095726@stu.xjtu.edu.cn; mzj620196@stu.xjtu.edu.cn; yangfengtao@stu.xjtu.edu.cn; kobeismvp@stu.xjtu.edu.cn).

Color versions of one or more figures in this article are available at https://doi.org/10.1109/TPEL.2023.3291893.

Digital Object Identifier 10.1109/TPEL.2023.3291893

I. INTRODUCTION

HIGH power density is the goal of power electronic converters. Switching frequency and speed are essential indicators for the converter to achieve high power density. Although Si insulated gate bipolar transistors (IGBTs) and SiC MOSFETs have the same turn-ON process that can achieve the same steep rise edge (or same rise time), Si IGBTs have a slower turn-OFF speed due to the trailing current. In addition, the body diode of SiC

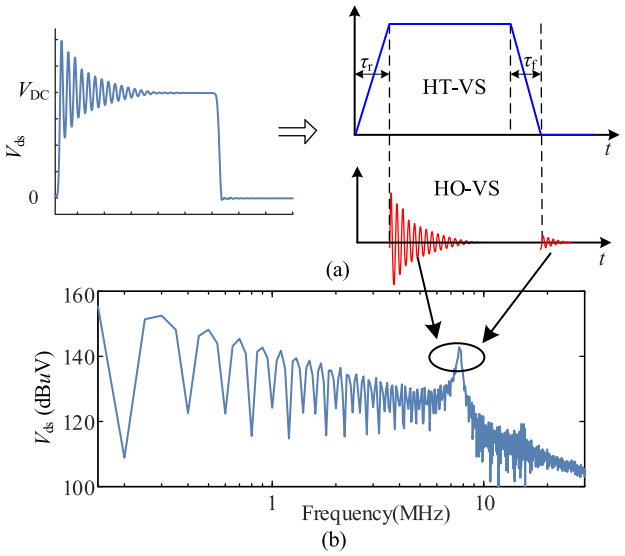

Fig. 1. Time-domain waveform and frequency-domain spectrum of voltage NS. (a) Time-domain waveform of H-VS divided into HT-VS and HO-VS. (b) Spectrum of the H-VS.

MOSFETs or SiC SBDs can reduce the reverse recovery current, thus further reducing the switching loss [1]. Therefore, SiC MOSFETs and SiC SBDs are more suitable for high-frequency converters.

However, the wide-bandgap power devices aggravate switching oscillation [2], [3]. The voltage waveform and current waveform of power devices are the important noise sources (NS) causing electromagnetic interference (EMI). The power device is replaced by a voltage waveform or current waveform in the common mode (CM) circuit model through the substitution principle [4], [5], [6], [7]. It is a common method to treat the power device as a black box and replace the whole power device with a voltage source or a current source [6], [7]. Because voltage and current waveforms can be measured directly, the analysis of NS is clearer.

The distinctions in EMI between SiC MOSFETs and Si IGBTs are mainly attributable to the switching frequency, oscillation, and slew rate (dv/dt) [8], [9], [10]. The high-frequency voltage noise source (H-VS) can be divided into the high-frequency trapezoidal voltage noise source (HT-VS) and the high-frequency switching oscillation voltage noise source (HO-VS) [11]. The HT-VS contains three pieces of information, namely, voltage rising edge, voltage falling edge, and switching frequency. The HO-VS includes high-frequency switching oscillations, as shown in Fig. 1.

The conducted CM current generated by HT-VS is independent of the parasitic inductance of the power module. Therefore, most existing studies directly ignore the parasitic inductances of power modules when establishing an EMI model and use HT-VS instead of the active power device to establish an EMI model [6], [7], [12], [13], [14], [15]. The HT-VS is compared between the SiC MOSFET and the Si IGBT in [9]. Only the switching frequency has a significant effect on HT-VS. Therefore, the existing EMI models and suppression methods for IGBTs can also be used for SiC MOSFETs, including passive filters, active filters, topology, modulation, balancing, and CM noise cancellation [16], [17], [18], [19], [20], [21]. These methods are designed for EMI caused by HT-VS. It should be noted that SiC MOSFETs have higher requirements for EMI suppression due to their higher switching frequency [16]. Therefore, the new packaging structure is also used for EMI suppression purposes. Reducing CM capacitance is the idea behind new packaging structures, such as the structure of an integrated CM screen layer and local shielding techniques [22], [23].

However, the high-frequency switching oscillation conduction common-mode (HO-CM) current caused by HO-VS cannot be ignored in the converters based on wide-bandgap devices, as shown in Fig. 1 [10], [11], [24]. The HO-CM current is determined by both the high-frequency switching oscillation noise source (HO-S) and the propagation path. The frequency domain of HO-VS has been analyzed and predicted [10], [11]. The propagation path of the HO-VS is dependent on the parasitic parameters of the power module. Obviously, the existing EMI models for IGBTs are not suitable for SiC MOSFETs with switching oscillation. Therefore, the HO-CM current model considering parasitic parameters is necessary.

There are few studies about the HO-CM model. The CM circuit is given considering all parasitic parameters given in [25], [26], and [27]. The simulation and experiment are compared in [25]. But the expression of HO-CM is not given. Xie et al. [26] established differential mode (DM) and CM models considering all parasitic parameters based on MATLAB. It is concluded that the effect of parasitic inductances on the EMI propagation path is weak due to the limitations of the analysis.

HO-CM current suppression methods are necessary in addition to passive filters. The volume of a high-frequency passive filter is larger due to the decline of magnetic core performance at high frequency and the filtering performance also decreases due to parasitic capacitances [16].

At present, due to the lack of an HO-CM model, HO-CM current suppression methods mainly focus on the oscillation NS itself rather than the propagation path. These methods can be divided into three categories: reducing parasitic inductance, increasing damping, and changing drive speed. The new packaging structure is the primary method to reduce parasitic inductance. Ren et al. [28] and Cougo et al. [29] proposed the adjacent decoupling concept using several decoupling capacitors to reduce the size of the commutation loop. Li et al. [30] presented a compact GaN power module with low parasitic parameters. Packaging structures with low module parasitic inductance often have more complex structures [22], [29], [31], [32], [33]. Therefore, the new packaging structure cannot consider both practicability and performance at present. Increasing the damping of the commutation loop is an effective method to suppress oscillation. Wu et al. [24] analyzed the impact of adding an *RC* snubber on switching oscillation and high-frequency EMI noise. An analytical method for *RC* snubber optimization design to eliminate switching oscillations is proposed [34]. However, adding an *RC* damping will increase converter system losses. Reducing the switching speed can also minimize switching oscillation while driving. The compromise between EMI and switching losses is

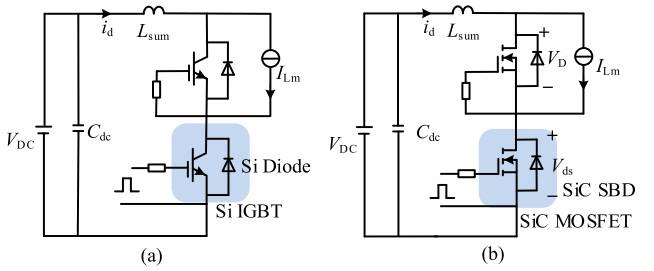

Fig. 2. Schematic diagram of the DPT circuit based on different power devices. (a) Si IGBT and Si diode. (b) SiC MOSFET and SiC SBD.

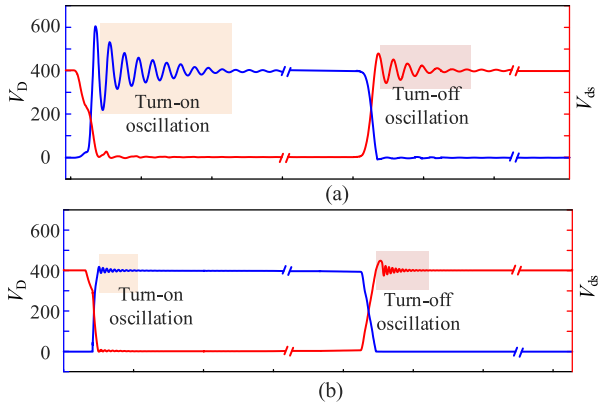

Fig. 3. Comparison of switching waveforms of SiC MOSFET and Si IGBT. (a) SiC MOSFET. (b) Si IGBT.

investigated by increasing the driving resistance [35]. The active gate drives have also been extensively studied to change *dv/dt* or *di/dt* [36], [37].

In order to link HO-S and HO-CM current, the frequency-domain expressions of the conducting path excited by HO-VS and high-frequency switching oscillation current noise source (HO-CS) considering parasitic parameters during turn-ON and turn-OFF are derived by using the Thevenin theorem and the Norton theorem, respectively, in this article. The HO-CS is selected as the main NS instead of HO-VS because it is continuous and contains both turn-ON and turn-OFF oscillations. The optimization principle of HO-CM current excited by HO-CS is proposed using the parasitic parameter of the power module itself. The proposed suppression method can guide the selection and design of power modules for different converters based on a half-bridge structure.

The rest of this article is organized as follows. Section II analyzes the factors affecting the HO-CM current, including HO-VS, HO-CS, and conducting path. In Sections III and IV, the conducting paths excited by HO-VS and HO-CS are deduced during turn-ON and turn-OFF oscillations, respectively, and the principle of HO-CM current cancellation is given. Experiments are verified by comparing two different power modules in Section V. Finally, Section VI concludes this article.

II. Analysis of Effect Factors of Conduction CM Current

The factors affecting the conducted CM current include NS, conducting path, and the affected objects. In a power converter, the NS is generated by the power devices during the switching process. The conducting path is related to the parasitic parameters of the power module. The line impedance stabilization network (LISN) is the affected object.

A. NS Analysis

The performance of power devices and peripheral circuits are key factors affecting NSs. In this section, the switching waveforms are compared with different power devices, the parasitic inductance of the commutation loop, and the driving resistance, representing the different device performances and the application of the power circuit and drive circuit.

1) Comparison of SiC Mosfet and Si IGBT: Fig. 2 shows the test schematic diagram of Si IGBT and SiC MOSFET based on the double-pulse test (DPT) circuit. In the following switching process, the lower device is the active test device to control the switching process.

Fig. 3 shows the comparison of the switching waveforms of SiC MOSFET and Si IGBT with the same driving resistance and parasitic inductance. It can be seen from Fig. 3 that the voltage oscillation of SiC MOSFET is more severe than that of Si IGBT during the switching process. Therefore, all SiC power devices without reverse recovery current cause more serious HO-VS than Si power devices.

In addition, Fig. 3 also contains two pieces of information. One is that the upper device voltage V_D oscillates during turn-ON, and the other is that the lower device voltage V_{ds} oscillates during turn-OFF. Therefore, the sum of the upper and lower device voltages is not equal to the dc voltage due to parasitic inductance during the oscillation process. However, the equivalent NS of the traditional CM model only uses the voltage waveform of the lower device or upper device, which ignores the oscillation of the turn-ON or turn-OFF process [10], [11], [14], [38]. Therefore, selecting only one voltage waveform to analyze the HO-VS is inaccurate. Fortunately, the HO-VS and HO-CS are a pair of oscillations. The waveform of HO-CS contains high-frequency oscillation during turn-ON and turn-OFF. The new combination of switching waveforms as NSs is given in Section II-B.

2) Comparison of Different Driving Resistances and Parasitic Inductances: Fig. 4 shows the switching waveform of reducing parasitic inductance or increasing driving resistance based on Fig. 3(a).

Reducing parasitic inductance can significantly reduce voltage oscillation without any sacrifice. Advanced packaging technology, such as three-dimensional packaging modules without bonding wire, can significantly reduce parasitic inductance. However, considering the cost and technology, the power module structure of commercial SiC MOSFET is still the same as that of Si IGBT. For example, the SiC MOSFET power module FF3MR12KM1P and the Si IGBT power module DF300R12KE3 from Infineon have the same structure and layout. Therefore, the influence of the parasitic inductance of SiC MOSFET power module on the switch waveform cannot be ignored.

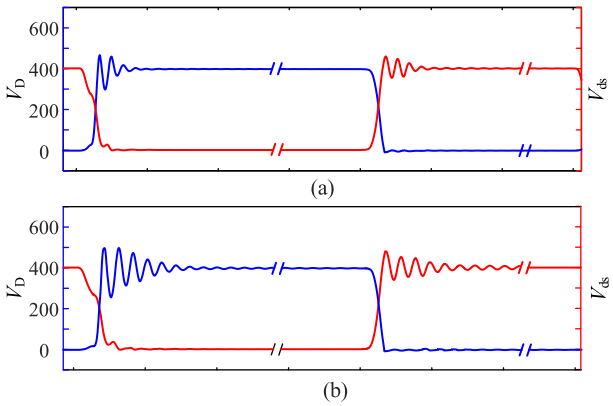

Fig. 4. Switching waveforms of reducing parasitic inductance or increasing driving resistance based on Fig. 3. (a) Reducing parasitic inductance. (b) Increasing drive resistance.

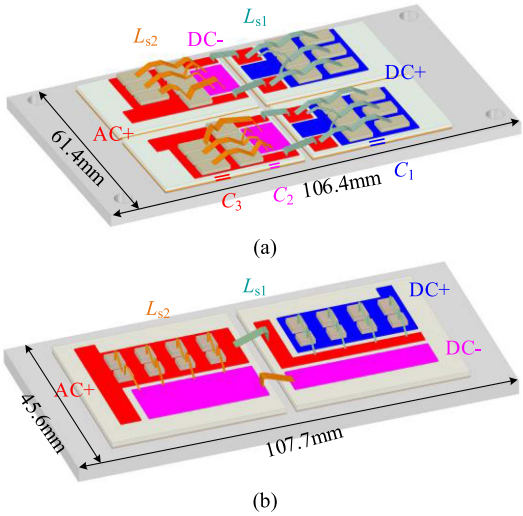

Fig. 5. Layout comparison of different power modules. (a) CAS300M12BM2 from CREE. (b) BSM120D12P2C005 from ROHM.

Increasing the driving resistance can also reduce the voltage oscillation but increase the switching loss. Switching oscillation still exists whether the parasitic inductance is reduced or the driving resistance increases.

B. Conducting Path Model

The conducting path is related to the parasitic parameters of the power module. Fig. 5 shows a comparison of the different layout structures CAS300M12BM2 from CREE and BSM120D12P2C005 from ROHM; note that the terminals of dc+, ac, and dc− are not shown. According to the structure layout, the half-bridge power module contains four parasitic inductances and three parasitic capacitances. Table I lists the parasitic parameters of the power module extracted by Q3D.

When considering the heatsink and LISN, the equivalent circuit diagram based on the DPT circuit can be obtained, as shown in Fig. 6(a). The inductance L_0 includes CM filter inductance and line parasitic inductance.

TABLE I
PARASITIC INDUCTANCES AND CAPACITANCES OF CAS300M12BM2 AND BSM120D12P2C005

CAS300M12BM2 (pF, nH)				BSM120D12P2C005 (pF, nH)			
L_{s1}	2.7	C_1	154	L_{s1}	6.6	C_1	56
L_{s2}	0.5	C_2	36	L_{s2}	9.7	C_2	80
L_1	6	C_3	182	L_1	3	C_3	102
L_2	6			L_2	3		

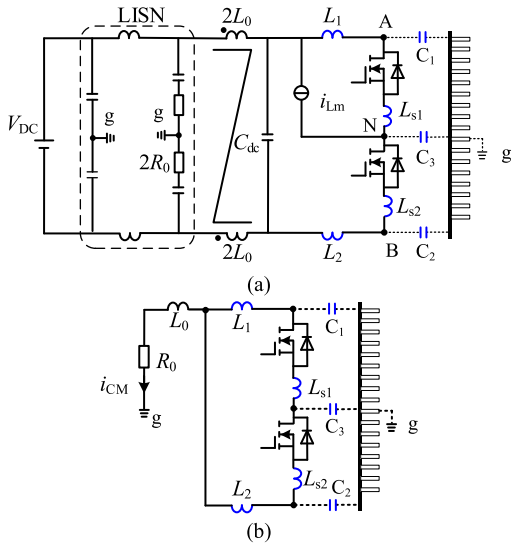

Fig. 6. Conducted EMI circuit diagram based on the DPT circuit. (a) EMI circuit. (b) CM high-frequency circuit.

The NSs include a dc voltage source, a current source, and power devices. The dc voltage and decoupling capacitance C_{dc} can be considered short circuits, and the current source can be considered an open circuit at a high frequency. Therefore, the equivalent high-frequency circuit can be obtained as shown in Fig. 6(b).

According to the equivalent high-frequency circuit, there are two power devices. The two devices can be equivalent to a current and a voltage source, respectively.

The L_{sum} and C_D form a resonant circuit during the turn-ON oscillation, and the lower devices are fully conducted simultaneously. Therefore, the upper device can be regarded as HO-CS, and the lower device can be regarded as HO-VS (this combination is called LVHC), as shown in Fig. 7(a). Similarly, the lower device can be regarded as HO-CS. The upper devices can be regarded as HO-VS during turn-OFF (this combination is called LCHV), as shown in Fig. 7(b).

If the influence of HO-CM current on HO-CS is not considered, the HO-CS i_D and i_d would be the same measuring points during switching oscillation due to the series connection. The spectrum of HO-CS i_d or i_D contains high-frequency oscillation during turn-ON and turn-OFF. Therefore, the HO-CS is selected as the main NS instead of HO-VS in the following section.

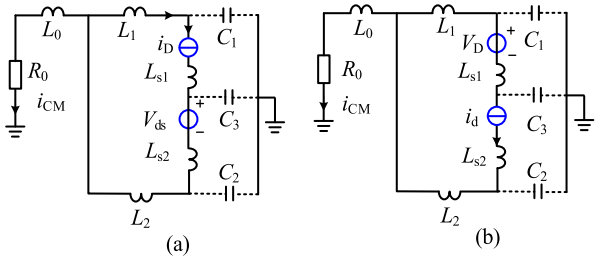

Fig. 7. CM high-frequency equivalent circuit for switching oscillation. (a) Turn-ON oscillation. (b) Turn-OFF oscillation.

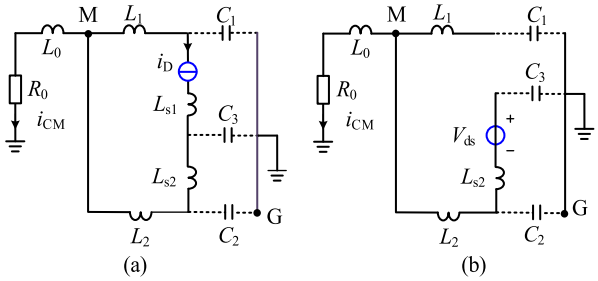

Fig. 8. CM high-frequency circuit during turn-ON oscillation. (a) Equivalent circuit excited by HO-CS. (b) Equivalent circuit excited by HO-VS.

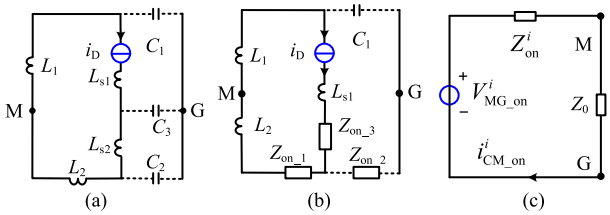

Fig. 9. Simplified process of the Thevenin equivalent circuit excited by HO-CS during turn-ON oscillation. (a) High-frequency equivalent circuit. (b) Intermediate process of the Thevenin equivalent circuit. (c) Thevenin's equivalent circuit.

III. Analysis of HO-CM Current During Turn-ON Oscillation

According to the superposition theorem, the circuit shown in Fig. 7(a) can be divided into CM circuits excited by HO-CS and HO-VS respectively, as shown in Fig. 8.

A. Analysis of Conducting Path Excited by HO-CS

The open-circuit voltage and output impedance excited by the HO-CS at the MG point can be obtained by using the Thevenin theorem, as shown in Fig. 9.

The impedances $Z_{\text{on\_1}}$, $Z_{\text{on\_2}}$, and $Z_{\text{on\_3}}$ in Fig. 9(b) can be obtained by $\Delta-\text{Y}$ transformation, as shown in Fig. 10.

$$\begin{cases} Z_{\text{on\_1}} = Z_{\text{L}_{\text{s2}}} Z_{\text{C}_2} / (Z_{\text{L}_{\text{s2}}} + Z_{\text{C}_2} + Z_{\text{C}_3}) \\ Z_{\text{on\_2}} = Z_{\text{C}_2} Z_{\text{C}_3} / (Z_{\text{L}_{\text{s2}}} + Z_{\text{C}_2} + Z_{\text{C}_3}) \\ Z_{\text{on\_3}} = Z_{\text{L}_{\text{s2}}} Z_{\text{C}_3} / (Z_{\text{L}_{\text{s2}}} + Z_{\text{C}_2} + Z_{\text{C}_3}) \end{cases} . \quad (1)$$

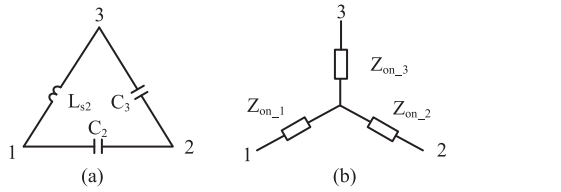

Fig. 10. Δ–Y impedance transformation. (a) Δ impedance. (b) Y impedance.

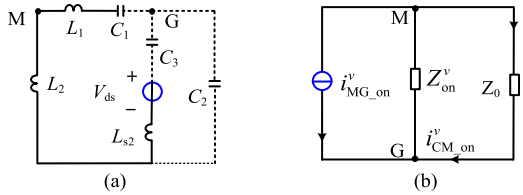

Fig. 11. Simplified process of the Norton equivalent circuit excited by HO-VS during turn-ON oscillation. (a) High-frequency equivalent circuit. (b) Norton equivalent circuit.

The open-circuit voltage $V^i_{\text{MG\_on}}$ and equivalent impedance $Z^i_{\text{on}}(s)$can be obtained from Fig. 9.

$$\begin{cases} V^i_{\text{MG\_on}} = \frac{(Z_{\text{on\_2}}+Z_{\text{C}_1})Z_{\text{L}_1} - (Z_{\text{L}_1}+Z_{\text{L}_2}+Z_{\text{on\_1}})Z_{\text{C}_1}}{Z_{\text{L}_1}+Z_{\text{L}_2}+Z_{\text{on\_1}}+Z_{\text{on\_2}}+Z_{\text{C}_1}} i_{\text{D}} \\ Z^i_{\text{on}}(s) = (Z_{\text{L}_2} + Z_{\text{on\_1}} + Z_{\text{on\_2}}) // (Z_{\text{L}_1} + Z_{\text{C}_1}) \end{cases} . \quad (2)$$

According to Fig. 9 and (2), the transfer function from HO-CS to HO-CM current can be obtained as follows:

$$\begin{aligned} \frac{I^i_{CM\_\text{on}}}{I_{\text{D}}} = G^i_{\text{on}} &= \frac{V^i_{\text{MG\_on}}}{(Z^i_{\text{on}}(s) + Z_0) I_{\text{D}}} \\ &= \frac{-s^2(s^2 H_1 + J_1)}{s^6 A_1 + s^5 B_1 + s^4 D_1 + s^3 E_1 + s^2 F_1 + s G_1 + 1} \end{aligned} \quad (3)$$

where

$$\begin{cases} A_1 = L_{s2} C_1 C_2 C_3 (L_0 L_{12} + L_1 L_2) \\ B_1 = R_0 L_{12} L_{s2} C_1 C_2 C_3 \\ \text{D}_1 = L_{s1} C_3 (L_1 C_1 + L_2 C_2 + L_0 C_{13}) \\ \qquad + (L_0 L_{12} + L_1 L_2) C_1 C_{23} \\ \text{E}_1 = R_0 (L_{12} C_1 C_{23} + L_{s2} C_{12} C_3) \\ F_1 = L_1 C_1 + L_{s2} C_3 + L_2 C_{23} + L_0 C_{123} \\ G_1 = R_0 C_{123} \\ H_1 = L_2 L_{s2} C_2 C_3 \\ J_1 = L_{s2} C_3 + L_2 C_{23} - L_1 C_1 \end{cases} . \quad (4)$$

The numerator of G^i_{on} has a corner frequency $\omega_{\text{n1\_on}}$. According to the Appendix, the corner frequency satisfies (5), which is independent of inductance L_0.

$$\omega_{\text{n1\_on}} = \sqrt{|J_1|/H_1} > \omega_{\text{res\_on}} \quad (5)$$

B. Analysis of Conducting Path Excited by HO-VS

Similarly, the short-circuit current and output impedance excited by the HO-VS at the MG point can be obtained by using the Norton theorem, as shown in Fig. 11.

The short-circuit current $I^v_{\mathrm{MG\_on}}$ and equivalent impedance Z^v_{on} can be obtained from Fig. 11 as follows:

$$\begin{cases} I^v_{\mathrm{MG\_on}} = \frac{-V_{\mathrm{ds}}}{Z_{L_2}//Z_{C_2}+Z_{C_3}+Z_{L_{s2}}} \frac{Z_{C_2}}{Z_{L_2}+Z_{C_2}} \\ Z^v_{\mathrm{on}}(s) = (Z_{L_1}+Z_{C_1})//((Z_{C_3}+Z_{L_{s2}})//Z_{C_2}+Z_{L_2}) \end{cases}. \tag{6}$$

According to Fig. 11 and formula (6), the transfer function from HO-VS to HO-CM current can be obtained as follows:

$$\begin{aligned} \frac{I^v_{\mathrm{CM\_on}}}{V_{\mathrm{ds}}} = G^v_{\mathrm{on}} &= \frac{I^v_{\mathrm{MG\_on}} Z^{\mathrm{v}}_{\mathrm{on}}(s)}{(Z^v_{\mathrm{on}}(s)+Z_0)V_{\mathrm{ds}}} \\ &= \frac{-s(s^2K_1+M_1)}{s^6A_1+s^5B_1+s^4D_1+s^3E_1+s^2F_1+sG_1+1} \end{aligned} \tag{7}$$

where

$$\begin{cases} K_1 = L_1C_1C_3 \\ M_1 = C_3 \end{cases}. \tag{8}$$

The denominator of G^i_{on} and G^v_{on}, which is determined by the parameters of the network, is the same. The numerator of G^v_{on} also has a resonant frequency $\omega_{\mathrm{n2\_on}}$, which is independent of inductance L_0.

$$\omega_{\mathrm{n2\_on}} = \sqrt{M_1/K_1} > \omega_{\mathrm{res\_on}}. \tag{9}$$

C. HO-CM Current Optimization Principle

When the inductive impedance of L_0 at the resonant frequency is much less than R_0, the denominator of G^i_{on} has two resonant frequencies $\omega_{\mathrm{d1\_on}}$ and $\omega_{\mathrm{d2\_on}}$ according to the second-order system. According to the Appendix, the resonant frequency satisfies (10) without considering the CM filter inductance.

$$\begin{cases} \omega_{\mathrm{d1\_on}} = \sqrt{G_1/E_1} > \omega_{\mathrm{res\_on}} \\ \omega_{\mathrm{d2\_on}} = \sqrt{E_1/B_1} > \omega_{\mathrm{res\_on}} \end{cases}. \tag{10}$$

When L_0 is a CM filter inductance, it is much larger than the parasitic inductance. The resonance frequency of the denominator of G^i_{on} will change. Fortunately, the resonant frequency of the numerator of G^i_{on} and G^v_{on} is constant, which will be applied to the HO-CM optimization principle. Therefore, the CM filter inductance is no longer considered.

When considering the propagation path below the resonant frequency $\omega_{\mathrm{res\_on}}$, the conducting path excited by HO-CS and HO-VS can be approximately equal to (11) during turn-ON oscillation without considering the CM filter inductance.

$$\begin{cases} \frac{I^i_{CM\_on}}{I_{\mathrm{D}}} = G^i_{\mathrm{on}} \approx -s^2J_1 = -s^2(L_{s2}C_3+L_2C_{23}-L_1C_1) \\ \frac{I^v_{\mathrm{CM\_on}}}{V_{\mathrm{ds}}} = G^v_{\mathrm{on}} \approx -sM_1 = -sC_3 \end{cases}. \tag{11}$$

The Bode diagram of the conducting path excited by HO-VS and HO-CS can be obtained by MATLAB. Fig. 12 shows the frequency-domain comparison of the accurate conducting path and approximate conducting path excited by HO-CS and HO-VS, respectively. The amplitude of the approximate conducting path is almost the same as the accurate conducting path, but the phase lags δ.

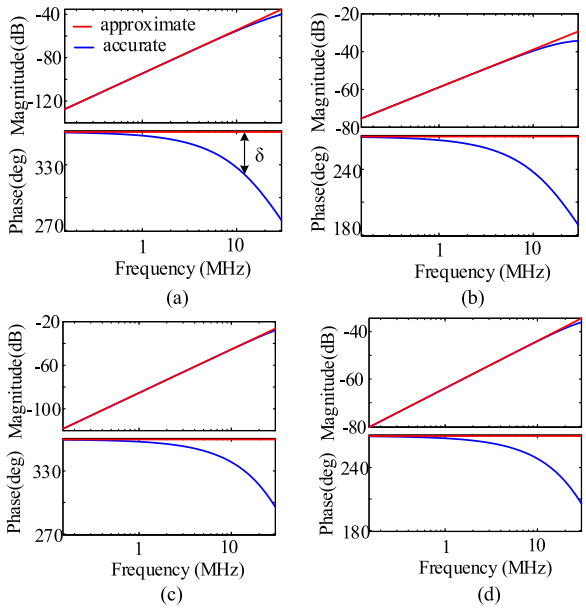

Fig. 12. Comparison of the accurate conducting path and the approximate conducting path excited by HO-CS and HO-VS during turn-ON oscillation. (a) G^i_{on} of CAS300M12BM2. (b) G^v_{on} of CAS300M12BM2. (c) G^i_{on} of BSM120D12P2C005. (d) G^v_{on} of BSM120D12P2C005.

It can be seen from (11) and (12) that the conducting path excited by the HO-VS is not affected by the parasitic inductances of the power modules, and it is only related to C_3 and $R_{\mathrm{ds\_on}}$. Therefore, the traditional CM model can ignore the effect of parasitic inductances on conducted CM current without considering the switching waveform oscillation. However, the conducting path excited by HO-CS is very sensitive to the parasitic inductances of the power modules.

To quantify the propagation path excited by HO-CS and HO-VS, the relationship between lower device voltage V_{ds} and upper device current i_{D} is given as follows:

$$V_{\mathrm{ds}} \approx R_{\mathrm{on\_ds}} i_{\mathrm{D}}. \tag{12}$$

where $R_{\mathrm{on\_ds}}$ is the ON-resistance of the power device. $R_{\mathrm{on\_ds}}$ of CAS300M12BM2 is 5 mΩ. $R_{\mathrm{on\_ds}}$ of BSM120D12P2C005 is 20 mΩ. The following equation can be obtained by substituting (12) into (11).

$$\frac{I^v_{\mathrm{CM\_on}}}{I_{\mathrm{D}}} = R_{\mathrm{on\_ds}} G^v_{\mathrm{on}} \approx -sR_{\mathrm{on\_ds}}M_1 = -sR_{\mathrm{on\_ds}}C_3. \tag{13}$$

Fig. 13 shows the amplitude of the conducting path excited by HO-VS and HO-CS during turn-ON oscillation. The frequency-domain amplitude of the conducting path excited by HO-CS is larger than that of HO-VS at the resonance frequency. Therefore, the effect excited by HO-VS on HO-CM can be ignored, but the HO-CM current excited by the HO-CS cannot be ignored during turn-ON oscillation. The propagation path amplitude of CAS300M12BM2 excited by HO-CS is 7 dB smaller than that of BSM120D12P2C005 during turn-ON oscillation, as shown in Fig. 13. That means the HO-CM current of CAS300M12BM2 is smaller than that of BSM120D12P2C005 with the same HO-CS during turn-ON oscillation.

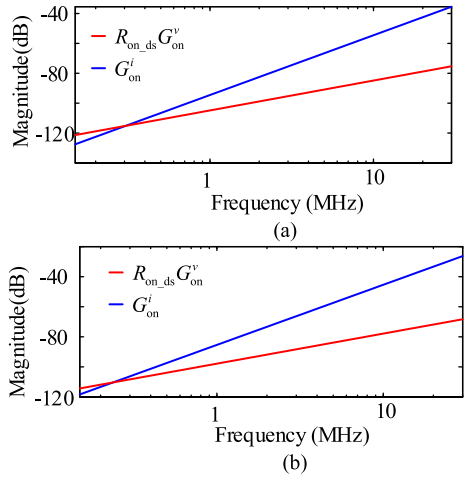

Fig. 13. Amplitude of the conducting path excited by HO-CS and HO-VS during turn-ON oscillation. (a) CAS300M12BM2. (b) BSM120D12P2C005.

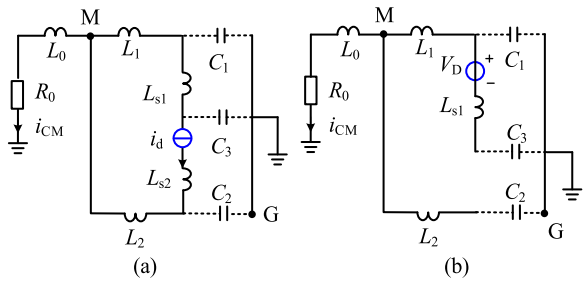

Fig. 14. CM high-frequency circuit based on the DPT circuit during turn-OFF oscillation. (a) Equivalent circuit excited by HO-CS. (b) Equivalent circuit excited by HO-VS.

The propagation path expression G^{i}_{on} contains two pieces of information: phase and amplitude. When J1>0, the HO-CM current lags HO-CS $|-\varphi|$. When J1<0, the HO-CM current leads the HO-CS $|180-\varphi|$. When J1 = 0, the HO-CM current can be completely canceled. For the convenience of experimental comparison, L_{s1} and C_3 are taken as the reference values of parasitic inductances and capacitances, respectively. The constraint of complete cancellation of HO-CM current can be obtained during turn-ON oscillation according to (11), which is independent of parasitic inductance L_{s1} during turn-ON oscillation.

$$qp_1 - (qm+1)p_2 = p_3. \tag{14}$$

IV. Analysis of HO-CM Current During Turn-OFF Oscillation

According to the superposition theorem, the circuit shown in Fig. 7(b) can be divided into two equivalent circuits excited by HO-CS and HO-VS, respectively, as shown in Fig. 14.

A. Analysis of Conducting Path Excited by HO-CS

Like the turn-ON process, the open-circuit voltage and output impedance excited by the HO-CS at the MG point can be obtained by using the Thevenin theorem, as shown in Fig. 15.

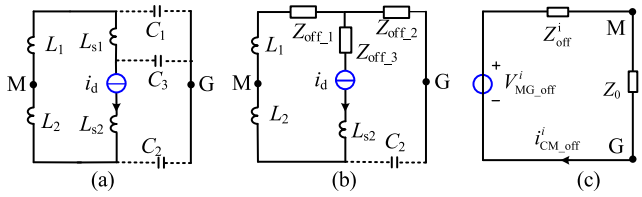

Fig. 15. Simplified process of the Thevenin equivalent circuit excited by HO-CS during turn-OFF oscillation. (a) High-frequency equivalent circuit. (b) Intermediate process of the Thevenin equivalent circuit. (c) Thevenin equivalent circuit.

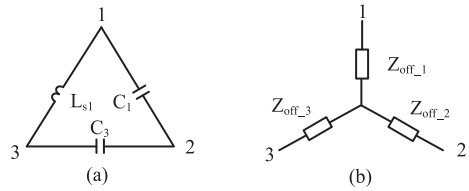

Fig. 16. $\Delta - Y$ impedance transformation. (a) Δ impedance. (b) Y impedance.

The impedances $R_{\text{off\_1}}$, $R_{\text{off\_2}}$, and $R_{\text{off\_3}}$, as shown in Fig. 15(b), can be obtained by $\Delta - Y$ transformation, as shown in Fig. 16.

$$\begin{cases} Z_{\text{off\_1}} = Z_{\text{L}_{\text{s1}}} Z_{\text{C}_1} / (Z_{\text{L}_{\text{s1}}} + Z_{\text{C}_1} + Z_{\text{C}_3}) \\ Z_{\text{off\_2}} = Z_{\text{C}_1} Z_{\text{C}_3} / (Z_{\text{L}_{\text{s1}}} + Z_{\text{C}_1} + Z_{\text{C}_3}) \\ Z_{\text{off\_3}} = Z_{\text{L}_{\text{s1}}} Z_{\text{C}_3} / (Z_{\text{L}_{\text{s1}}} + Z_{\text{C}_1} + Z_{\text{C}_3}) \end{cases}. \tag{15}$$

From Fig. 15, the open-circuit voltage $V^{i}_{\text{MG\_off}}$ and equivalent impedance Z^{i}_{off} can be obtained as follows:

$$\begin{cases} V^{i}_{\text{MG\_off}} = \frac{(Z_{\text{off\_2}} + Z_{\text{C}_2}) Z_{\text{L}_2} - (Z_{\text{L}_1} + Z_{\text{L}_2} + Z_{\text{off\_1}}) Z_{\text{C}_3}}{Z_{\text{L}_1} + Z_{\text{L}_2} + Z_{\text{off\_1}} + Z_{\text{off\_2}} + Z_{\text{C}_2}} (-I_{\text{d}}) \\ Z^{i}_{\text{off}}(s) = (Z_{\text{L}_1} + Z_{\text{off\_1}} + Z_{\text{off\_2}}) // (Z_{\text{L}_2} + Z_{\text{C}_2}) \end{cases}. \tag{16}$$

Using Fig. 15 and (16), the transfer function from HO-CS to HO-CM current can be obtained as follows:

$$\begin{aligned} G^{i}_{\text{off}} &= \frac{I^{i}_{CM\_\text{off}}}{I_{\text{d}}} = \frac{V^{i}_{\text{MG\_off}}}{(Z^{i}_{\text{off}}(s) + Z_0) I_{\text{d}}} \\ &= \frac{s^2 (s^2 H_2 + J_2)}{s^6 A_2 + s^5 B_2 + s^4 D_2 + s^3 E_2 + s^2 F_2 + s G_2 + 1} \end{aligned} \tag{17}$$

where

$$\begin{cases} A_2 = L_{\text{s1}} C_1 C_2 C_3 (L_0 L_{12} + L_1 L_2) \\ B_2 = R_0 L_{12} L_{\text{s1}} C_1 C_2 C_3 \\ \text{D}_2 = L_{\text{s1}} C_3 (L_1 C_1 + L_2 C_2 + L_0 C_{12}) \\ \qquad + (L_0 L_{12} + L_1 L_2) C_{13} C_2 \\ \text{E}_2 = R_0 (L_{12} C_{13} C_3 + L_{\text{s1}} C_{12} C_3) \\ F_2 = L_2 C_2 + L_{\text{s1}} C_3 + L_1 C_{13} + L_0 C_{123} \\ G_2 = R_0 C_{123} \\ H_2 = L_1 L_{\text{s1}} C_1 C_3 \\ J_2 = L_{\text{s1}} C_3 + L_1 C_{13} - L_2 C_2 \end{cases}. \tag{18}$$

The numerator of G^{i}_{off} has a corner frequency $\omega_{\text{n1\_off}}$. According to the Appendix, the corner frequency satisfies the formula

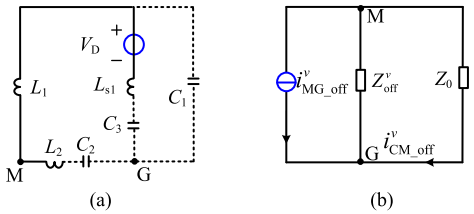

Fig. 17. Simplified process of the Norton equivalent circuit excited by HO-VS during turn-OFF oscillation. (a) High-frequency equivalent circuit. (b) Norton equivalent circuit.

(19), which is also independent of inductance L_0.

$$\omega_{n1\_off} = \sqrt{|J_2|/H_2} > \omega_{res\_off}. \tag{19}$$

B. Analysis of Conducting Path Excited by HO-VS

Similarly, the short-circuit current and output impedance excited by HO-VS at the MG point can be obtained by using the Norton theorem, as shown in Fig. 17.

The short-circuit current $I^v_{MG\_off}$ and equivalent impedance $Z^v_{off}(s)$ can be obtained from Fig. 17.

$$\begin{cases} I^v_{MG\_off} = \dfrac{V_D}{Z_{L_1}//Z_{C_1}+Z_{C_3}+Z_{L_{s1}}} \dfrac{Z_{C_1}}{Z_{L_1}+Z_{C_1}} \\ Z^v_{off}(s) = (Z_{L_2}+Z_{C_2})//((Z_{C_3}+Z_{L_{s1}})//Z_{C_1}+Z_{L_1}) \end{cases}. \tag{20}$$

Using Fig. 17 and (20), the transfer function from HO-VS to HO-CM current can be obtained as follows:

$$\begin{aligned} G^v_{off} &= \frac{I^v_{CM\_off}}{V_D} = \frac{I^v_{MG\_off} Z^v_{off}(s)}{(Z^i_{off}(s)+Z_0)V_D} \\ &= \frac{s(s^2K_2+M_2)}{s^6A_2+s^5B_2+s^4D_2+s^3E_2+s^2F_2+sG_2+1} \end{aligned} \tag{21}$$

where

$$\begin{cases} K_2 = L_2C_2C_3 \\ M_2 = C_3 \end{cases}. \tag{22}$$

The numerator of G^v_{off} has a resonant frequency ω_{n2_off}, which is also independent of inductance L_0.

$$\omega_{n2\_off} = \sqrt{M_2/K_2} > \omega_{res\_off}. \tag{23}$$

C. HO-CM Current Optimization Principle

The denominator of G^i_{off} and G^v_{off} has two resonant frequencies ω_{d1_off} and ω_{d2_off} without considering the CM filter inductance. The resonant frequency satisfies the following equation, according to the Appendix.

$$\begin{cases} \omega_{d1\_off} = \sqrt{G_2/E_2} > \omega_{res\_off} \\ \omega_{d2\_off} = \sqrt{E_2/B_2} > \omega_{res\_off} \end{cases}. \tag{24}$$

When considering the propagation path below the resonant frequency ω_{res_off}, the amplitude of the conducting path excited by HO-CS and HO-VS can be approximately equal to (25) during turn-OFF oscillation.

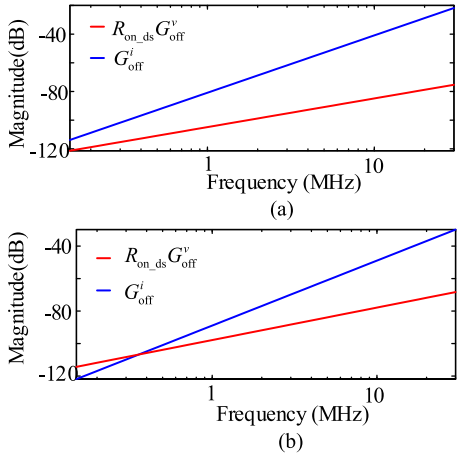

Fig. 18. Amplitude of the conducting path excited by HO-CS and HO-VS during turn-OFF oscillation. (a) CAS300M12BM2. (b) BSM120D12P2C005.

$$\begin{cases} \frac{I^i_{MG\_off}}{I_d} = G^i_{off} \approx s^2J_2 = s^2(L_{s1}C_3 + L_1C_{13} - L_2C_2) \\ \frac{I^v_{MG\_off}}{I_d} = R_{ds\_on}G^v_{off} \approx sR_{ds\_on}M_2 = sR_{ds\_on}C_3 \end{cases}. \tag{25}$$

It is similar to the conducting path excited by HO-VS and HO-CS during turn-ON oscillation. The amplitude of the approximate conducting path (25) is almost the same as the accurate conducting path (17), except for the phase lags φ. The effect excited by HO-VS on HO-CM can be ignored, but the HO-CM current excited by the HO-CS cannot be ignored during turn-OFF oscillation, as shown in Fig. 18. The propagation path amplitude of BSM120D12P2C005 excited by HO-CS is 7 dB smaller than that of CAS300M12BM2 during turn-OFF oscillation, as shown in Fig. 18. That means the HO-CM current of BSM120D12P2C005 is smaller than that of CAS300M12BM2 with the same HO-CS during turn-OFF oscillation.

When J2 > 0, the HO-CM current leads HO-CS 180-φ. When J2 < 0, the HO-CM current generated lags the HO-CS $|-\varphi|$. When J2 $= 0$, the HO-CM current can be completely canceled.

Similar to turn-ON oscillation, the constraint of complete cancellation of HO-CM current can be obtained during turn-OFF oscillation according to (25), which is independent of parasitic inductance L_{s2} during turn-OFF oscillation.

$$p_2qm - p_1(q+1) = 1. \tag{26}$$

V. Experimental Verifications

In order to verify the principle of HO-CM current cancellation and compare the effect of parasitic parameters of power modules on HO-CM current, two power modules, CAS300M12BM2 and BSM120D12P2C005, with different parasitic inductances L_1 and L_2 are tested in this article.

A. Experimental Platform

The experimental platform based on the DPT circuit was built, as shown in Fig. 19. The decoupling capacitors are composed of three 22-nF multilayer ceramic chip capacitors and a 10-μF

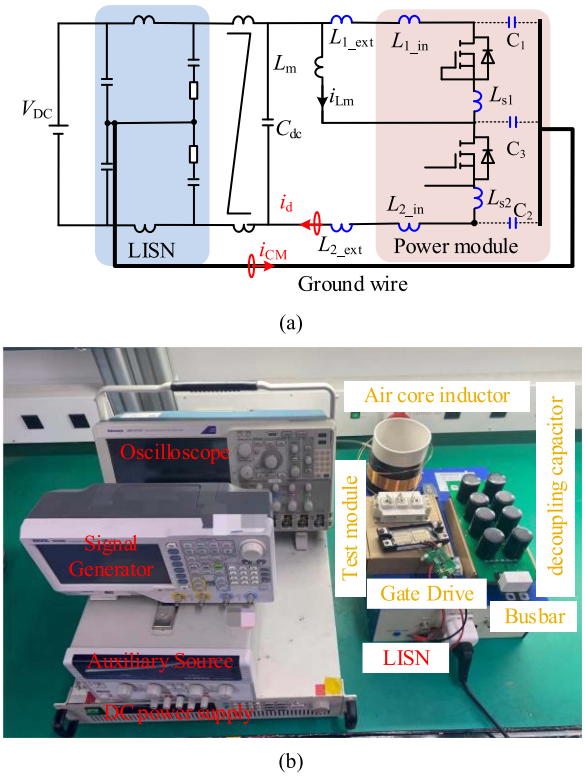

Fig. 19. Experimental test platform. (a) Schematic diagram of the DPT circuit. (b) DPT experimental platform.

metalized polypropylene film capacitor in parallel. The parasitic parameters of the two power modules have been extracted by ANSYS Q3D, as listed in Table I. L_1 and L_2 include the parasitic inductances of the power modules themselves, L_{1_in} and L_{2_in}, and the Busbar L_{1_ext} and L_{2_ext}, as expressed in (27) by per unit. The Busbar parasitic inductances are the only controllable variables for commercial modules.

$$\begin{cases} p_1 = p_{1\_ext} + p_{1\_in} \\ p_2 = p_{2\_ext} + p_{2\_in} \end{cases}. \tag{27}$$

The LISN can provide a CM current path and stable high-frequency impedance. Due to the short operation time of the DPT circuit, the EMI receiver cannot be used. The HO-CS and HO-CM currents are obtained by the current Probe TCP0030, and then fast Fourier transform analysis is carried out with MATLAB.

In order to analyze the impact excited by HO-CS on HO-CM current during turn-ON and turn-OFF, respectively, the driver chip UCC5390SC from TI is selected, which has split output.

B. Experiment of Power Module CAS300M12BM2

The constraint conditions on HO-CM current cancellation of parasitic parameters L_{1_ext} and L_{2_ext} of power module CAS300M12BM2 during turn-ON oscillation and turn-OFF oscillation can be obtained by substituting (27) into (14) and (26), respectively.

$$p_{1\_ext} = 1.4p_{2\_ext} + 1.11 \tag{28}$$

TABLE II
EXPERIMENTAL CONDITIONS AND NUMBERS OF CAS300M12BM2

	No1	No2	No3	No4	No5
p_{1_ext} (L_{1_ext})	10 (27 nH)	13.7 (37 nH)	17 (47 nH)	17 (47 nH)	17 (47 nH)
p_{2_ext} (L_{2_ext})	17 (47 nH)	13.7 (37 nH)	10 (27 nH)	10 (27 nH)	10 (27 nH)
R_{g_on}	9.1 Ω	9.1 Ω	9.1 Ω	9.1 Ω	47 Ω
R_{g_off}	47 Ω	47 Ω	47 Ω	9.1 Ω	9.1 Ω
V_{DC}	50 V	50 V	50 V	400 V	400 V

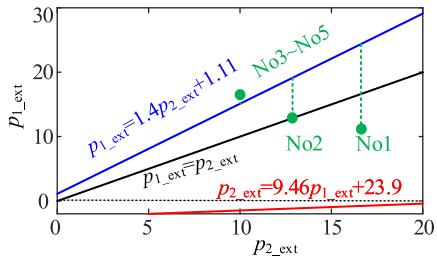

Fig. 20. HO-CM cancellation constraint line and experiment numbers of CAS300M12BM2.

$$p_{2\_ext} = 9.46p_{1\_ext} + 23.9. \tag{29}$$

When p_{2_ext} is equal to 0, p_{1_ext} is required to be equal to 1.11 during turn-ON oscillation. When p_{1_ext} is equal to 0, p_{2_ext} is required to be equal to 23.9 during turn-OFF oscillation. The difference between p_{1_ext} and p_{2_ext} represents the asymmetry of Busbar. Therefore, the HO-CM cancellation during turn-OFF oscillation is more difficult than that during turn-ON oscillation. The power module CAS300M12BM2 is used to verify HO-CM current cancellation during turn-ON oscillation.

In order to analyze the influence of parasitic parameters on HO-CM current during turn-ON oscillation, the following two conditions need to be met at the same time.

1) HO-S remains unchanged during turn-ON oscillation, which can be achieved by ensuring that the sum of p_{1_ext} and p_{2_ext} remains unchanged.
2) HO-S does not exist during turn-OFF oscillation, which can be achieved by a large turn-OFF resistance and a small load current. The larger turn-OFF resistance and smaller load current can reduce the switching speed, thus reducing turn-OFF oscillation [39].

The experimental conditions and numbers of CAS300M12BM2 are listed in Table II. Fig. 20 shows the HO-CM cancellation constraint line marked with the experiment numbers.

Fig. 21 shows the time- and frequency-domain waveforms of HO-CS and HO-CM current of CAS300M12BM2 with No1–No3 during the switching process. The sum of parasitic inductances of the power circuit and the gate driving resistance from No1 to No3 is the same, so the time-domain and frequency-domain waveforms of the HO-CS are almost the same, as shown in Fig. 21(a)–(c). In addition, compared with the HO-CS during turn-ON, the HO-CS during turn-OFF can be ignored. However,

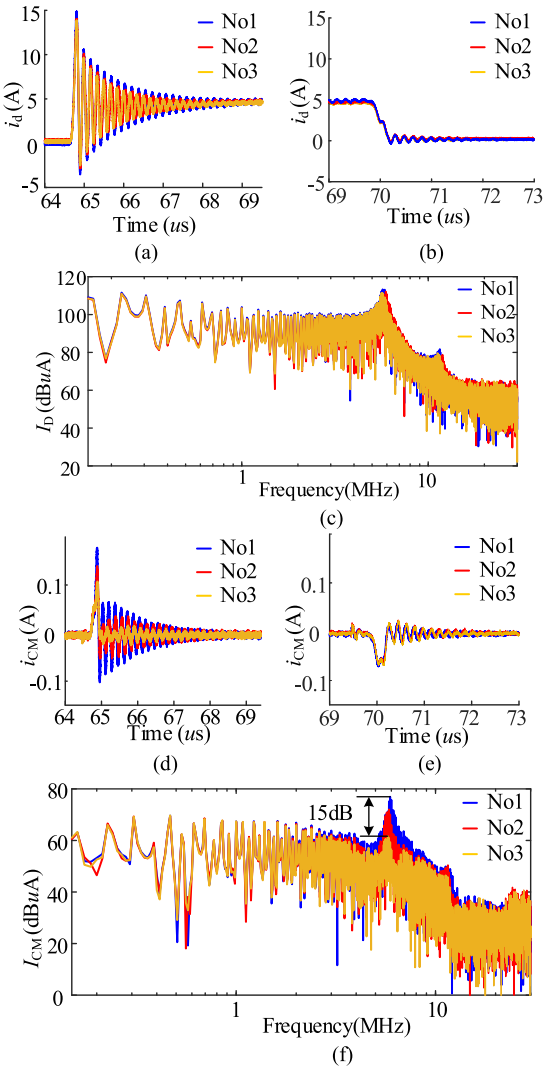

Fig. 21. Time- and frequency-domain waveforms of HO-CS and HO-CM current of CAS300M12BM2 with No1 to No3 during turn-ON. (a) Time-domain waveforms of HO-CS during turn-ON. (b) Time-domain waveforms of HO-CS during turn-OFF. (c) Frequency-domain waveforms of HO-CS. (d) Time-domain waveforms of HO-CM current during turn-ON. (e) Time-domain waveforms of HO-CM current during turn-OFF. (f) Frequency-domain waveforms of HO-CM current.

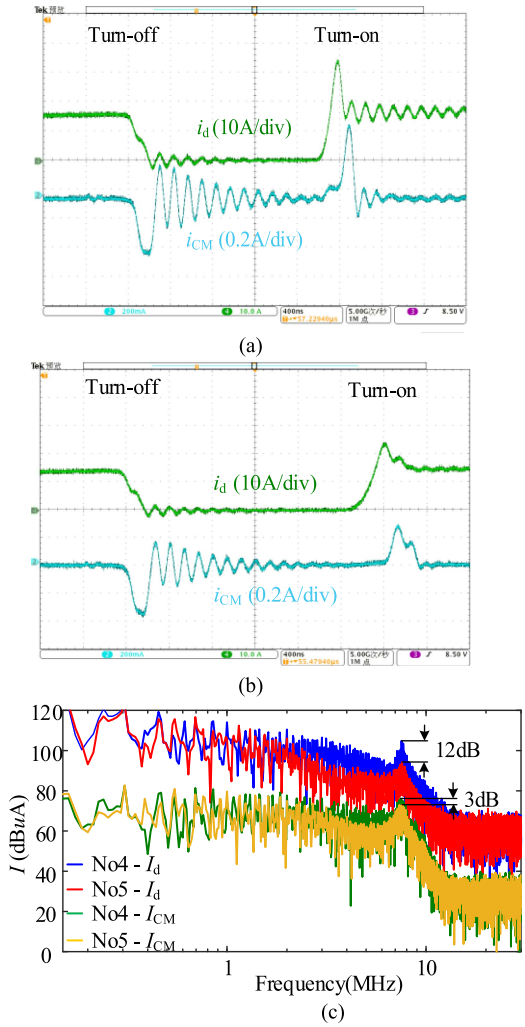

Fig. 22. Time- and frequency-domain waveforms of HO-CS and HO-CM current of CAS300M12BM2 with No4 and No5 during turn-ON. (a) Time-domain waveforms of HO-CS and HO-CM current with No4. (b) Time-domain waveforms of HO-CS and HO-CM current with No5. (c) Frequency-domain waveforms of HO-CS and HO-CM current with No4 and No5.

the HO-CM current is different during turn-ON due to different positions of parasitic inductances. No3 has minimum HO-CM current and No1 has maximum HO-CM current, as shown in Fig. 21(d), which is consistent with Fig. 20. The HO-CM spectrum of No3 is 15 dB lower than that of No1. The HO-CM optimization principle can effectively reduce HO-CM current during turn-on oscillation.

The HO-CM optimization principle during turn-ON oscillation is further verified, as shown in Fig. 22.

Fig. 22 shows the comparison of the effects of different turn-ON driving resistances on HO-CM current with No4 and No5. No4 has a smaller turn-ON driving resistance than No5, and therefore, there is switching oscillation during turn-ON. Although the HO-CS spectrum of No4 is 12 dB higher than that of No5, the HO-CM current spectrum of No4 is only 3 dB higher than that of No5. Therefore, the HO-CS has little effect on the HO-CM current during turn-ON oscillation by the cancellation method proposed in this article.

C. *Experiment of Power Module BSM120D12P2C005*

Similar to CAS300M12BM2, the constraint conditions on HO-CM current cancellation of parasitic parameters L_{1_ext} and L_{2_ext} of power module BSM120D12P2C005 during turn-ON oscillation and turn-OFF oscillation can be obtained by substituting (27) into (14) and (26), respectively.

$$p_{1\_ext} = 3.32p_{2\_ext} + 3.7 \tag{30}$$

$$p_{2\_ext} = 1.98p_{1\_ext} + 1.72. \tag{31}$$

The HO-CM cancellation during turn-OFF oscillation is easier than that during turn-ON oscillation. The power module BSM120D12P2C005 is used to verify HO-CM current cancellation during turn-OFF oscillation.

TABLE III
EXPERIMENTAL CONDITIONS AND NUMBERS OF BSM120D12P2C005

	No6	No7	No8	No9	No10
p_{1_ext} (L_{1_ext})	3.8 (25 nH)	1.8 (12 nH)	0.3 (2 nH)	0.3 (2 nH)	0.3 (2 nH)
p_{2_ext} (L_{2_ext})	0.3 (2 nH)	2.7 (18 nH)	4.1 (27 nH)	3.8 (25 nH)	4.1 (27 nH)
R_{g_on}	47 Ω	47 Ω	47 Ω	9.1 Ω	9.1 Ω
R_{g_off}	9.1 Ω	9.1 Ω	9.1 Ω	9.1 Ω	47 Ω
V_{DC}	50 V	50 V	50 V	400 V	400 V

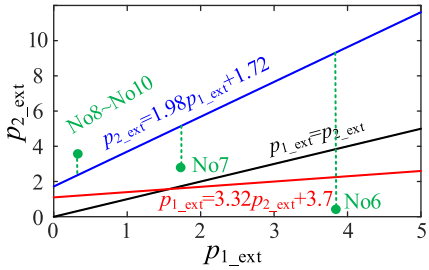

Fig. 23. HO-CM cancellation constraint line and experiment numbers of BSM120D12P2C005.

Similar to CAS300M12BM2, the following two conditions need to be met to analyze the influence of parasitic parameters on HO-CM current during turn-OFF oscillation.

1) HO-S remains unchanged during turn-OFF oscillation.
2) HO-S does not exist during turn-ON oscillation, which can be achieved by a large turn-ON resistance and a small load current.

The experimental conditions and numbers of BSM120D12P2C005 are listed in Table III. Fig. 23 shows the HO-CM cancellation constraint line marked with the experiment numbers.

Fig. 24 shows the time- and frequency-domain waveforms of HO-CS and HO-CM current of BSM120D12P2C005 with No6–No8 during the switching process. The sum of parasitic inductances of the power circuit and the gate driving resistance from No6 to No8 is the same, and therefore, the time-domain and frequency-domain waveforms of the HO-CS are almost the same, as shown in Fig. 24(a)–(c). In addition, compared with the HO-CS during turn-OFF, the HO-CS during turn-ON can be ignored. However, the HO-CM current is different during turn-OFF due to different positions of parasitic inductances. No8 has a minimum HO-CM current, and No6 has a maximum HO-CM current, as shown in Fig. 24(e), which is consistent with Fig. 23. The HO-CM spectrum of No8 is 7.5 dB lower than that of No6. The HO-CM optimization principle is effective in reducing HO-CM current during turn-OFF oscillation.

The HO-CM optimization principle during turn-OFF oscillation is further verified, as shown in Fig. 25.

Fig. 25 shows the comparison of the effects of different turn-OFF driving resistances on HO-CM current with No9 and No10. No9 has a smaller turn-ON driving resistance than No10, so there is switching oscillation during turn-OFF. Although the

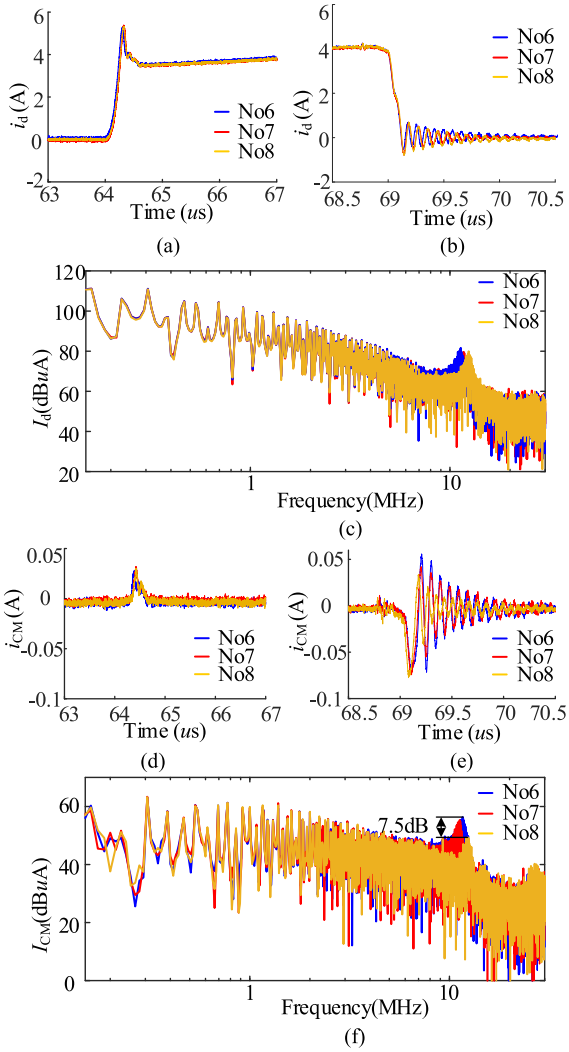

Fig. 24. Time- and frequency-domain waveforms of HO-CS and HO-CM current of BSM120D12P2C005 with No6–No8 during turn-OFF. (a) Time-domain waveforms of HO-CS during turn-ON. (b) Time-domain waveforms of HO-CS during turn-OFF. (c) Frequency-domain waveforms of HO-CS. (d) Time-domain waveforms of HO-CM current during turn-ON. (e) Time-domain waveforms of HO-CM current during turn-OFF. (f) Frequency-domain waveforms of HO-CM current.

HO-CS spectrum of No9 is 6 dB higher than that of No10, the HO-CM current spectrum of No9 and No10 is the same. Therefore, the HO-CS has little effect on the HO-CM current during turn-OFF oscillation by the cancellation method proposed in this article.

D. Comparison of HO-CM Current Between Two Power Modules

The most significant difference between the two power modules is the layout of parasitic capacitances C_1, C_2, and C_3, which leads to different HO-CM current characteristics during turn-ON and turn-OFF oscillations.

The constraint of HO-CM current cancellation cannot be met simultaneously during turn-ON and turn-OFF. The power

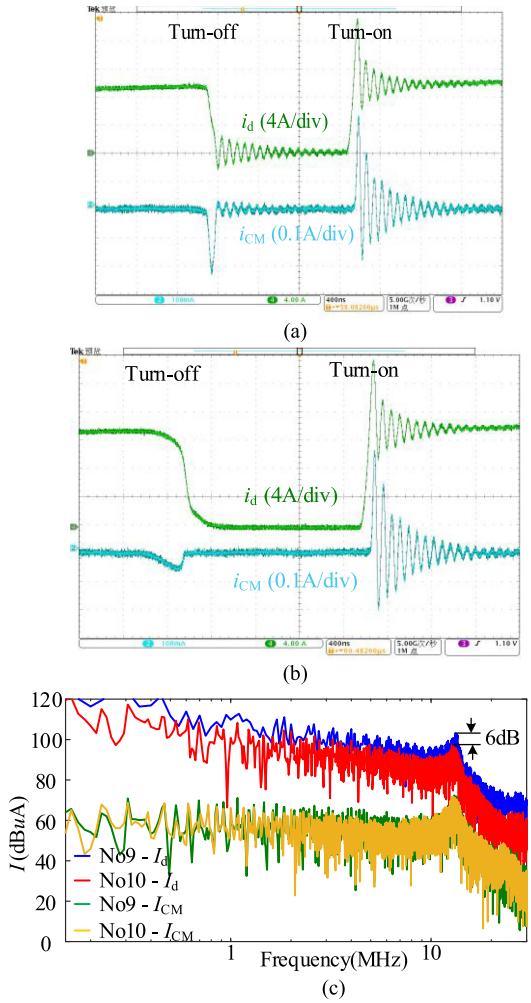

Fig. 25. Time- and frequency-domain waveforms of HO-CS and HO-CM current of BSM120D12P2C005 with No9 and No10 during turn-OFF. (a) Time-domain waveforms of HO-CS and HO-CM current with No9. (b) Time-domain waveforms of HO-CS and HO-CM current with No10. (c) Frequency-domain waveforms of HO-CS and HO-CM current with No9 and No10.

module CAS300M12BM2 can realize HO-CM current cancellation more easily than BSM120D12P2C005 during turn-ON oscillation considering the symmetrical design of parasitic inductances L_1 and L_2 of Busbar. The power module BSM120D12P2C005 can realize HO-CM current cancellation more easily than CAS300M12BM2 during turn-OFF oscillation.

In the experiment, the combination of parasitic inductances L_{1_ext} and L_{2_ext} of No3 and No8 is optimal during turn-ON and turn-OFF. There is a slight error between the experimental conditions and the ideal constraint, as shown in Figs. 20 and 23. The error of module BSM120D12P2C005 is greater than that of module CAS300M12BM2.

The error is mainly caused by the following reasons:

1) the measurement error of the parasitic inductance of Busbar,
2) the parasitic inductance of decoupling capacitance,
3) the error of equivalent parasitic inductances of the power modules.

TABLE IV
EXPERIMENTAL CONDITIONS AND NUMBERS OF BSM120D12P2C005 BASED ON DCM OR CRM BUCK CONVERTER

	p_{1_ext} (L_{1_ext})	p_{2_ext} (L_{2_ext})	R_{g_on}	R_{g_off}
No11	0.3 (2 nH)	4.1 (27 nH)	9.1 Ω	1.3 Ω
No12	4.1 (27 nH)	0.3 (2 nH)	9.1 Ω	1.3 Ω

Because the Busbar and decoupling capacitance are the same when testing the two power modules, the greater error of BSM120D12P2C005 is caused by the equivalent parasitic inductances of the power modules. Obviously, power module BSM120D12P2C005 has a more complex internal structure than CAS300M12BM2, as shown in Fig. 5.

Although the Busbar parasitic inductances are used to meet the HO-CM current cancellation constraint condition in the experiment, it can also be achieved by optimizing the power module layout. When the parasitic inductances of power modules and Busbar satisfy the constraint of HO-CM cancellation during turn-ON oscillation, we call it layout A. When the parasitic inductances of power modules and Busbar satisfy the constraint of HO-CM cancellation during turn-OFF oscillation, we call it layout B.

E. Case of Discontinuous Conduction Mode or Critical Conduction Mode Buck Converter

The first switching cycle of the DPT circuit can simulate the critical conduction mode (CRM) or discontinuous conduction mode (DCM) buck converter, which is a typical soft turn-ON and hard turn-OFF converter. Therefore, layout B is suitable for the CRM or DCM buck converter to reduce HO-CM current during turn-OFF oscillation. The power module BSM120D12P2C005 can meet the requirements of layout B by designing Busbar parasitic inductances.

The experimental conditions and numbers of BSM120D12P2C005 based on DCM or CRM buck converter are listed in Table IV. Fig. 26 shows the time- and frequency-domain waveforms of HO-CS and HO-CM current of BSM120D12P2C005 with No11 and No12. There are almost no HO-CS during turn-ON due to zero-current turn-ON. The HO-CS is mainly generated during turn-OFF, as shown in Fig. 26(a). Time-domain and frequency-domain waveforms of the HO-CS are almost the same due to the same driving resistance and the sum of parasitic inductances. However, due to the HO-CM cancellation principle, the HO-CM spectrum of No11 is 13 dB lower than that of No12. Therefore, the HO-CM current based on layout B is hardly affected by HO-CS during turn-OFF oscillation.

VI. CONCLUSION

This article deduces the CM mathematical model considering the parasitic parameters of the power module, and the effects of parasitic parameters on the propagation paths excited by HO-VS and HO-CS are analyzed during turn-ON and turn-OFF oscillations, respectively. Under the combination of LVHC during

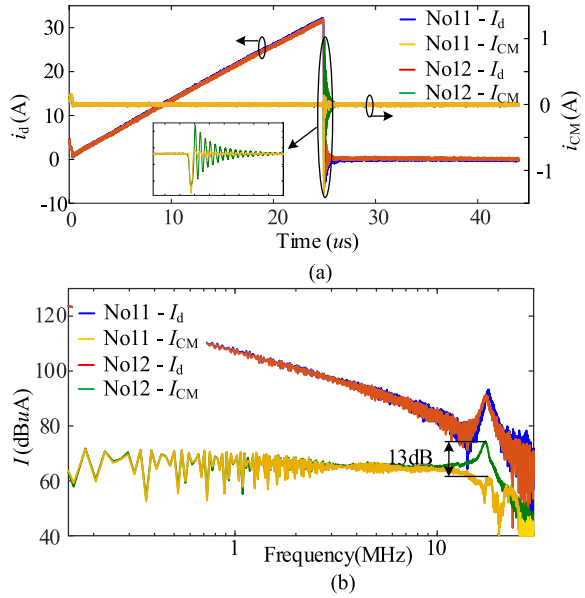

Fig. 26. Time- and frequency-domain waveforms of HO-CS and HO-CM current of BSM120D12P2C005 with No11 and No12 based on DCM or CRM buck converter. (a) Time-domain waveforms of HO-CS and HO-CM current. (b) Frequency-domain waveforms of HO-CS and HO-CM current.

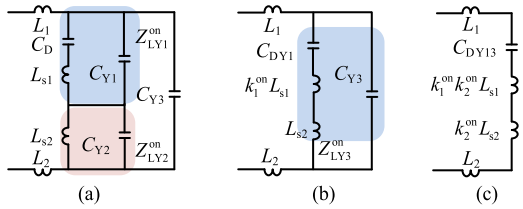

Fig. 27. Simplified process of the schematic diagram during turn-ON oscillation.

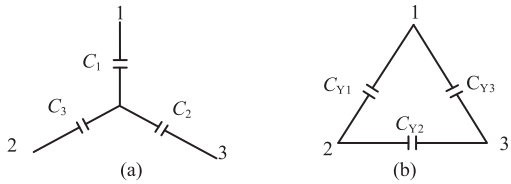

Fig. 28. Y–△ impedance transformation. (a) Y impedance. (b) △ impedance.

turn-ON and LCHV during turn-OFF, the effect excited by HO-VS on HO-CM current is almost only related to parasitic capacitance C_3, whereas the effect excited by HO-CS on HO-CM current is related to all parasitic parameters, including L_1, L_2, L_{s1}, L_{s1}, C_1, C_2, and C_3. Therefore, the effect of parasitic parameters on HO-CM current cannot be ignored, which is often not considered in most CM models. According to the propagation path excited by HO-CS, the HO-CM current optimization principle is proposed during turn-ON and turn-OFF oscillations, respectively. The transfer function from HO-CS to HO-CM includes all parasitic parameters related to the power module layout.

The different phenomena of HO-CM current can be observed by exchanging only parasitic inductances L_1 and L_2 without changing the sum of parasitic inductances in the experiment. In order to reduce the HO-CM during turn-ON oscillation, the absolute value of J_1 related to the power module layout should be as small as possible. When the parasitic parameters of the power module meet constraint (14), the HO-CM current can almost be completely eliminated during turn-ON oscillation. Similarly, in order to reduce the HO-CM during turn-OFF oscillation, the absolute value of J_2 should also be as small as possible. When the parasitic parameters of the power module meet constraint (26), the HO-CM current can almost be completely eliminated during turn-OFF oscillation.

By comparing two power modules with different layouts, we can find that power module CAS300M12BM2 can realize HO-CM current cancellation more easily than BSM120D12P2C005 during turn-ON oscillation. The power module BSM120D12P2C005 can realize HO-CM current cancellation more easily than CAS300M12BM2 during turn-OFF oscillation. The HO-CM current spectrum of a DCM or CRM buck converter based on BSM120D12P2C005 can be reduced by more than 10 dB using the optimization principle. According to constraints, the analysis of the effect of power module parasitic parameters on HO-CM current can guide the layout design of power modules for different converters based on a half-bridge structure.

APPENDIX

Generally, the oscillation amplitude of HO-CM current is less than that of HO-CS, thus the effect of HO-CM current on HO-CS can be ignored. The oscillation schematic diagram can be obtained using the configuration shown in Fig. 7(a) during turn-ON oscillation and is shown in Fig. 27.

The impedances C_{Y1}, C_{Y2}, and C_{Y3} as shown in Fig. 27(a) can be obtained by Y–△ transformation, as shown in Fig. 28.

$$\begin{cases} Z_{C_{Y1}} = (Z_{C_1}Z_{C_2} + Z_{C_2}Z_{C_3} + Z_{C_3}Z_{C_1})/Z_{C_2} \\ Z_{C_{Y2}} = (Z_{C_1}Z_{C_2} + Z_{C_2}Z_{C_3} + Z_{C_3}Z_{C_1})/Z_{C_1} \\ Z_{C_{Y3}} = (Z_{C_1}Z_{C_2} + Z_{C_2}Z_{C_3} + Z_{C_3}Z_{C_1})/Z_{C_3} \end{cases}. \quad (32)$$

The relationship between C_{Y1}, C_{Y2}, and C_{Y3} can be obtained according to (32).

$$\begin{cases} C_{Y2} = mC_{Y1} \\ C_{Y3} = nC_{Y1} \end{cases}. \quad (33)$$

Therefore, Z^{on}_{LY1} and Z^{on}_{LY2} can be obtained in Fig. 27.

$$\begin{cases} Z^{on}_{LY1} = (Z_{C_D} + Z_{L_{s1}})//Z_{C_{Y1}} = \frac{s^2L_{s1}C_D+1}{s(s^2L_{s1}C_DC_{Y1}+C_D+C_{Y1})} \\ Z^{on}_{LY2} = Z_{L_{s2}}//Z_{C_{Y2}} = \frac{sL_{s2}}{s^2L_{s2}C_{Y2}+1} \end{cases}. \quad (34)$$

The relationship between the output capacitance C_D of the power devices and the parasitic capacitances C_{Y1} and C_{Y3} can be defined as follows:

$$\begin{cases} k^{on}_1 = \frac{C_D}{C_D+C_{Y1}} \\ k^{on}_2 = \frac{C_{DY1}}{C_{DY1}+C_{Y3}} = \frac{C_D+C_{Y1}}{C_D+(1+n)C_{Y1}} \end{cases}. \quad (35)$$

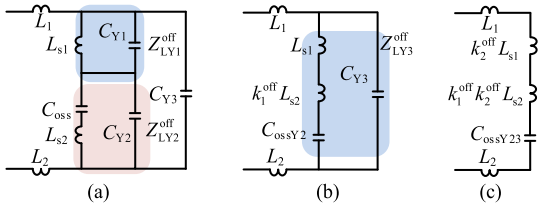

Fig. 29. Simplified process of the schematic diagram during turn-OFF oscillation.

Generally, C_{D} is greater than C_{Y1}, so (34) can be simplified as (36) below resonant frequency $\sqrt{L_{\mathrm{s1}}C_{\mathrm{Y1}}}$.

$$\begin{cases} Z_{\mathrm{LY1}}^{\mathrm{on}} \approx sL_{s1}k_1^{\mathrm{on}} + \frac{1}{s(C_{\mathrm{D}}+C_{\mathrm{Y1}})} \\ Z_{\mathrm{LY2}}^{\mathrm{on}} \approx sL_{s2} \end{cases}. \tag{36}$$

According to (36), Fig. 27(a) can be simplified to Fig. 27(b). Similarly, $Z_{\mathrm{LY3}}^{\mathrm{on}}$ can be obtained as shown in Fig. 27(b) and is given as follows:

$$Z_{\mathrm{LY3}}^{\mathrm{on}} \approx sk_2^{\mathrm{on}}(L_{s1}k_1^{\mathrm{on}} + L_{s2}) + \frac{1}{s(C_{\mathrm{D}} + C_{\mathrm{Y13}})}. \tag{37}$$

According to (37), Fig. 27(b) can be simplified to Fig. 27(c). Similar to the turn-ON oscillation, the oscillation schematic diagram can be obtained during the turn-OFF oscillation, as shown in Fig. 29.

$$\begin{cases} k_1^{\mathrm{off}} = \frac{C_{\mathrm{oss}}}{C_{\mathrm{oss}}+C_{\mathrm{Y2}}} = \frac{C_{\mathrm{oss}}}{C_{\mathrm{oss}}+mC_{\mathrm{Y1}}} \\ k_2^{\mathrm{off}} = \frac{C_{\mathrm{oss}}+C_{\mathrm{Y2}}}{C_{\mathrm{oss}}+C_{\mathrm{Y23}}} = \frac{C_{\mathrm{oss}}+mC_{\mathrm{Y1}}}{C_{\mathrm{oss}}+(m+n)C_{\mathrm{Y1}}} \\ Z_{\mathrm{LY1}}^{\mathrm{off}} \approx sL_{\mathrm{s1}} \\ Z_{\mathrm{LY2}}^{\mathrm{off}} \approx sL_{\mathrm{s2}}k_1^{\mathrm{off}} + \frac{1}{s(C_{\mathrm{oss}}+C_{\mathrm{Y2}})} \\ Z_{\mathrm{LY3}}^{\mathrm{off}} \approx sk_2^{\mathrm{off}}(L_{\mathrm{s2}}k_1^{\mathrm{off}} + L_{s1}) + \frac{1}{s(C_{\mathrm{oss}}+C_{\mathrm{Y23}})} \end{cases}. \tag{38}$$

Figs. 27(c) and 29(c) show the oscillation circuit formed by equivalent parasitic parameters during turn-ON oscillation and turn-OFF oscillation, respectively.

The resonant angular frequency can be obtained during turn-ON oscillation and turn-OFF oscillation, respectively, which may be a little different due to the parasitic parameters of the power module.

$$\begin{cases} \omega_{\mathrm{res\_on}} = \sqrt{\frac{1}{(L_{12}+k_1^{\mathrm{on}}k_2^{\mathrm{on}}L_{\mathrm{s1}}+k_2^{\mathrm{on}}L_{\mathrm{s2}})C_{\mathrm{DY13}}}} \\ \omega_{\mathrm{res\_off}} = \sqrt{\frac{1}{(L_{12}+k_2^{\mathrm{off}}L_{\mathrm{s1}}+k_1^{\mathrm{off}}k_2^{\mathrm{off}}L_{\mathrm{s1}})C_{\mathrm{ossY23}}}} \end{cases}. \tag{39}$$

REFERENCES

[1] N.-A. Parker-Allotey et al., "Conduction and switching loss comparison between an IGBT/Si-PiN diode pair and an IGBT/SiC-schottky diode pair," in *Proc. IEEE 2nd PES Int. Conf. Exhib. Innov. Smart Grid Technol.*, 2011, pp. 1–6.

[2] O. Alatise, N.-A. Parker-Allotey, D. Hamilton, and P. Mawby, "The impact of parasitic inductance on the performance of silicon-carbide Schottky barrier diodes," *IEEE Trans. Power Electron.*, vol. 27, no. 8, pp. 3826–3833, Aug. 2012, doi: 10.1109/tpel.2012.2183390.

[3] T. Liu, R. Ning, T. Wong, and Z. J. Shen, "Modeling and analysis of SiC MOSFET switching oscillations," *IEEE J. Emerg. Sel. Topics Power Electron.*, vol. 4, no. 3, pp. 3826–3833, Sep. 2016, doi: 10.1109/jestpe.2016.2587358.

[4] C. Marlier, A. Videt, N. Idir, H. Moussa, and R. Meuret, "Modeling of switching transients for frequency-domain EMC analysis of power converters," in *Proc. IEEE 15th Int. Power Electron. Motion Control Conf.*, 2012, pp. DS1e.1-1–DS1e.1-8, doi: 10.1109/EPEPEMC.2012.6397241.

[5] K. Takahashi, T. Ibuchi, and T. Funaki, "Noise-source model for frequency-domain EMI simulation of a single-phased power circuit," *IEEE Trans. Electromagn. Compat.*, vol. 63, no. 3, pp. 772–782, Jun. 2021, doi: 10.1109/temc.2020.3022887.

[6] H. Zhang, L. Yang, S. Wang, and J. Puukko, "Common-mode EMI noise modeling and reduction with balance technique for three-level neutral point clamped topology," *IEEE Trans. Ind. Electron.*, vol. 64, no. 9, pp. 7563–7573, Sep. 2017, doi: 10.1109/tie.2017.2677344.

[7] J. Wang, X. Liu, Y. Xun, and S. Yu, "Common mode noise reduction of three-level active neutral point clamped inverters with uncertain parasitic capacitance of photovoltaic panels," *IEEE Trans. Power Electron.*, vol. 35, no. 7, pp. 6974–6988, Jul. 2020, doi: 10.1109/tpel.2019.2956771.

[8] L. Zhang, X. Yuan, X. Wu, C. Shi, J. Zhang, and Y. Zhang, "Performance evaluation of high-power SiC MOSFET modules in comparison to Si IGBT modules," *IEEE Trans. Power Electron.*, vol. 34, no. 2, pp. 1181–1196, Feb. 2019, doi: 10.1109/tpel.2018.2834345.

[9] D. Han, S. Li, Y. Wu, W. Choi, and B. Sarlioglu, "Comparative analysis on conducted CM EMI emission of motor drives: WBG versus Si devices," *IEEE Trans. Ind. Electron.*, vol. 64, no. 10, pp. 8353–8363, Oct. 2017, doi: 10.1109/tie.2017.2681968.

[10] R. Zhang, W. Chen, Y. Zhou, Z. Shi, R. Yan, and X. Yang, "Mathematical modeling of EMI spectrum envelope based on switching transient behavior," *IEEE J. Emerg. Sel. Topics Power Electron.*, vol. 10, no. 2, pp. 2497–2515, Apr. 2022, doi: 10.1109/jestpe.2021.3109040.

[11] B. Hao, C. Peng, X. L. Tang, and Z. B. Zhao, "Calculation and analysis for spectrum characteristics parameters of switching device for reduced EMI generation," *IEEE Trans. Power Electron.*, vol. 37, no. 5, pp. 5444–5454, May 2022, doi: 10.1109/Tpel.2021.3126836.

[12] D. N. Dalal et al., "Impact of power module parasitic capacitances on medium-voltage SiC MOSFETs switching transients," *IEEE J. Emerg. Sel. Topics Power Electron.*, vol. 8, no. 1, pp. 298–310, Mar. 2020, doi: 10.1109/jestpe.2019.2939644.

[13] S. Wang, P. Kong, and F. C. Lee, "Common mode noise reduction for boost converters using general balance technique," *IEEE Trans. Power Electron.*, vol. 22, no. 4, pp. 1410–1416, Jul. 2007, doi: 10.1109/tpel.2007.900503.

[14] S. Karimi, E. Farjah, T. Ghanbari, F. Naseri, and J.-L. Schanen, "Estimation of parasitic capacitance of common mode noise in vehicular applications: An unscented Kalman filter-based approach," *IEEE Trans. Ind. Electron.*, vol. 68, no. 8, pp. 7526–7534, Aug. 2021, doi: 10.1109/tie.2020.3007088.

[15] E. Rondon-Pinilla, F. Morel, C. Vollaire, and J.-L. Schanen, "Modeling of a buck converter with a SiC JFET to predict EMC conducted emissions," *IEEE Trans. Power Electron.*, vol. 29, no. 5, pp. 2246–2260, May 2014, doi: 10.1109/tpel.2013.2295053.

[16] D. Han, C. T. Morris, W. Lee, and B. Sarlioglu, "Comparison between output CM chokes for SiC drive operating at 20- and 200-kHz switching frequencies," *IEEE Trans. Ind. Appl.*, vol. 53, no. 3, pp. 2178–2188, May/Jun. 2017, doi: 10.1109/tia.2017.2672919.

[17] Y. Zhou et al., "A novel neutral point based active EMI filter for common mode noise attenuation," *IEEE Trans. Power Electron.*, vol. 37, no. 9, pp. 10081–10085, Sep. 2022, doi: 10.1109/tpel.2022.3161288.

[18] C. T. Morris, D. Han, and B. Sarlioglu, "Reduction of common mode voltage and conducted EMI through three-phase inverter topology," *IEEE Trans. Power Electron.*, vol. 32, no. 3, pp. 1720–1724, Mar. 2017, doi: 10.1109/tpel.2016.2608388.

[19] S. Ohn, J. Yu, R. Burgos, D. Boroyevich, and H. Suryanarayana, "Reduced common-mode voltage PWM scheme for full-SiC three-level uninterruptible power supply with small DC-link capacitors," *IEEE Trans. Power Electron.*, vol. 35, no. 8, pp. 8638–8651, Aug. 2020, doi: 10.1109/tpel.2019.2962964.

[20] S. Wang, F. C. Lee, and Q. Li, "Improved balance technique for common-mode noise suppression of PCB-based PFC," *IEEE Trans. Power Electron.*, vol. 37, no. 4, pp. 4174–4182, Apr. 2022, doi: 10.1109/tpel.2021.3124505.

[21] L. Xie and X. Yuan, "Common-mode current reduction at DC and AC sides in inverter systems by passive cancellation," *IEEE Trans. Power Electron.*, vol. 36, no. 8, pp. 9069–9079, Aug. 2021, doi: 10.1109/tpel.2021.3058840.

[22] C. M. DiMarino, B. Mouawad, C. M. Johnson, D. Boroyevich, and R. Burgos, "10-kV SiC MOSFET power module with reduced common-mode noise and electric field," *IEEE Trans. Power Electron.*, vol. 35, no. 6, pp. 6050–6060, Jun. 2020, doi: 10.1109/tpel.2019.2952633.

[23] P. B. Derkacz, J.-L. Schanen, P.-O. Jeannin, P. J. Chrzan, P. Musznicki, and M. Petit, "EMI mitigation of GaN power inverter leg by local shielding techniques," *IEEE Trans. Power Electron.*, vol. 37, no. 10, pp. 11996–12004, Oct. 2022, doi: 10.1109/tpel.2022.3176943.
[24] Y. Wu, S. Yin, H. Li, and W. Ma, "Impact of RC snubber on switching oscillation damping of SiC MOSFET with analytical model," *IEEE J. Emerg. Sel. Topics Power Electron.*, vol. 8, no. 1, pp. 163–178, Mar. 2020, doi: 10.1109/jestpe.2019.2953272.
[25] M. Laour, R. Tahmi, and C. Vollaire, "Modeling and analysis of conducted and radiated emissions due to common mode current of a buck converter," *IEEE Trans. Electromagn. Compat.*, vol. 59, no. 4, pp. 1260–1267, Aug. 2017, doi: 10.1109/temc.2017.2651984.
[26] Y. Xie, C. Chen, Z. Z. Huang, T. Liu, Y. Kang, and F. Luo, "High frequency conducted EMI investigation on packaging and modulation for a SiC-based high frequency converter," *IEEE J. Emerg. Sel. Topics Power Electron.*, vol. 7, no. 3, pp. 1789–1804, Sep. 2019, doi: 10.1109/Jestpe.2019.2919349.
[27] W. Kim, C. Seng, J. Seo, and H. Cha, "High-frequency circuit modeling and analysis for common-mode noise voltage of a single-phase inverter," *J. Elect. Eng. Technol.*, vol. 17, no. 2, pp. 1239–1248, 2022, doi: 10.1007/s42835-021-00987-z.
[28] Y. Ren et al., "Voltage suppression in wire-bond-based multichip phase-leg SiC MOSFET module using adjacent decoupling concept," *IEEE Trans. Ind. Electron.*, vol. 64, no. 10, pp. 8235–8246, Oct. 2017, doi: 10.1109/tie.2017.2714149.
[29] B. Cougo, H. Sathler, R. Riva, V. Dos Santos, N. Roux, and B. Sareni, "Characterization of low inductance SiC module with integrated capacitors for aircraft applications requiring low losses and low EMI issues," *IEEE Trans. Power Electron.*, vol. 36, no. 7, pp. 8230–8242, Jul. 2021, doi: 10.1109/tpel.2020.3014529.
[30] B. Li, X. Yang, K. Wang, H. Zhu, L. Wang, and W. Chen, "A compact double-sided cooling 650V/30A GaN power module with low parasitic parameters," *IEEE Trans. Power Electron.*, vol. 37, no. 1, pp. 426–439, Jan. 2022, doi: 10.1109/tpel.2021.3092367.
[31] C. DiMarino et al., "Design and experimental validation of a wire-bond-less 10-kV SiC MOSFET power module," *IEEE J. Emerg. Sel. Topics Power Electron.*, vol. 8, no. 1, pp. 381–394, Mar. 2020, doi: 10.1109/jestpe.2019.2944138.
[32] A. I. Emon, Z. Yuan, A. Mirza, A. Deshpande, M. Ul Hassan, and F. Luo, "1200V/650V/160A SiC+Si IGBT 3L hybrid T-type NPC power module with enhanced EMI shielding," *IEEE Trans. Power Electron.*, vol. 36, no. 12, pp. 13660–13673, Dec. 2021, doi: 10.1109/tpel.2021.3089578.
[33] C. Yao et al., "Comparison study of common-mode noise and thermal performance for lateral wire-bonded and vertically integrated high power diode modules," *IEEE Trans. Power Electron.*, vol. 33, no. 12, pp. 10572–10582, Dec. 2018, doi: 10.1109/tpel.2018.2801336.
[34] X. Yang, M. Xu, Q. Li, Z. Wang, and M. He, "Analytical method for RC snubber optimization design to eliminate switching oscillations of SiC MOSFET," *IEEE Trans. Power Electron.*, vol. 37, no. 4, pp. 4672–4684, Apr. 2021, doi: 10.1109/tpel.2021.3127516.
[35] N. Oswald, P. Anthony, N. McNeill, and B. H. Stark, "An experimental investigation of the tradeoff between switching losses and EMI generation with hard-switched all-Si, Si-SiC, and all-SiC device combinations," *IEEE Trans. Power Electron.*, vol. 29, no. 5, pp. 2393–2407, May 2014, doi: 10.1109/tpel.2013.2278919.
[36] X. Wu, C. Wang, H. Zaman, X. Zhao, and X. Wu, "Variable gate voltage driving circuits for mitigation of coupling noise in silicon carbide MOSFET," *IEEE J. Emerg. Sel. Topics Power Electron.*, vol. 9, no. 6, pp. 6761–6772, Jun. 2021, doi: 10.1109/jestpe.2021.3061612.
[37] Y. Yang, Y. Wen, and Y. Gao, "A novel active gate driver for improving switching performance of high-power SiC MOSFET modules," *IEEE Trans. Power Electron.*, vol. 34, no. 8, pp. 7775–7787, Aug. 2019, doi: 10.1109/tpel.2018.2878779.
[38] D. Han, C. T. Morris, W. Lee, and B. Sarlioglu, "A case study on common mode electromagnetic interference characteristics of GaN HEMT and Si MOSFET power converters for EV/HEVs," *IEEE Trans. Transp. Electrific.*, vol. 3, no. 1, pp. 168–179, Mar. 2017, doi: 10.1109/tte.2016.2622005.
[39] S. K. Roy and K. Basu, "Analytical model to study hard turn off switching dynamics of SiC MOSFET and schottky diode pair," *IEEE Trans. Power Electron.*, vol. 36, no. 1, pp. 861–875, Jan. 2020, doi: 10.1109/tpel.2020.2998873.

Qingshou Yang (Student Member, IEEE) was born in Hebei, China, in 1993. He received the B.S. and M.S. degrees in electrical engineering and automation from Yanshan University, Qinhuangdao, China, in 2016 and 2019, respectively. He is currently working toward the Ph.D. degree in electrical engineering at Xi'an Jiaotong University, Xi'an, China.

His research interests include the application of wide-bandgap devices and power electronic integration.

Laili Wang (Senior Member, IEEE) received the B.S., M.S., and Ph.D. degrees from the School of Electrical Engineering, Xi'an Jiaotong University, Xi'an, China, in 2004, 2007, and 2011, respectively.

Since 2011, he has been a Postdoctoral Research Fellow with the Electrical Engineering Department, Queen's University, Kingston, ON, Canada. From 2014 to 2017, he was an Electrical Engineer with Sumida, Canada. In 2017, he joined Xi'an Jiaotong University as a full Professor. His research interests include packaging and integration, wireless power transfer, and energy harvesting.

Dr. Wang is an Associate Editor for the IEEE TRANSACTIONS ON POWER ELECTRONICS and the IEEE JOURNAL OF EMERGING AND SELECTED TOPICS IN POWER ELECTRONICS. He is the Vice Chair of the Technical Committee of Power Conversion Systems and Components in PELS, the Co-Chair of System Integration and Application in the International Technology Roadmap for Wide Band-Gap Power Semiconductor, and the Chair of the IEEE CPSS&PELS Joint Chapter in Xi'an, China.

Zhiyuan Qi (Student Member, IEEE) was born in Henan, China, in 1989. He received the B.S. and M.S. degrees in electrical engineering and automation from Harbin Engineering University, Harbin, China, in 2012 and 2015, respectively. He is currently working toward the Ph.D. degree in electrical engineering at Xi'an Jiaotong University, Xi'an, China.

His research interests include the packaging and integration of wide-bandgap power semiconductors and high-frequency power conversion technologies.

Xiaohui Lu (Student Member, IEEE) received the B.S. degree in electronic and electrical engineering in 2018 from Xi'an Jiaotong University, Xi'an, China, where he is currently working toward the Ph.D. degree in electronic and electrical engineering.

His current research interests include wide-bandgap semiconductor devices' reliability and high-temperature applications.

Zaojun Ma (Student Member, IEEE) was born in Gansu, China, in 1993. He received the B.S. and M.S. degrees in electrical engineering from the Harbin Institute of Technology, Harbin, China, in 2016 and 2018, respectively. He is currently working toward the Ph.D. degree in electrical engineering at Xi'an Jiaotong University, Xi'an, China.

His research interests include the packaging and application of wide-bandgap power semiconductor devices and pulsed power technologies.

Fengtao Yang (Student Member, IEEE) was born in Shandong, China, in 1994. He received the B.S. degree in electronic and electrical engineering from the China University of Mining and Technology, Xuzhou, China, in 2016. He is currently working toward the Ph.D. degree in electronic and electrical engineering at Xi'an Jiaotong University, Xi'an, China.

His current interests include advancements in electrical performance, thermal management, operation temperature, power density, and integration of power modules, especially in wide-bandgap semiconductor-device-based, high-current, high-temperature, high-frequency power conversion systems.

Haihua Wang (Student Member, IEEE) was born in 1990. He received the B.S. and M.S. degrees in electrical engineering in 2014 and 2017 from Xi'an Jiaotong University, Xi'an, China, where he is currently working toward the Ph.D. degree in electrical engineering.

His research interests include applications and packaging of wide-bandgap semiconductor devices and performance testing of SiC MOSFETs.